

# Studies of Functional Defects for Fast Na-Ion Conduction in $\text{Na}_{3-y}\text{PS}_{4-x}\text{Cl}_x$ with a Combined Experimental and Computational Approach

Xuyong Feng, Po-Hsiu Chien, Zhuoying Zhu, Iek-Heng Chu, Pengbo Wang, Marcello Immediato-Scuotto, Hesam Arabzadeh, Shyue Ping Ong, and Yan-Yan Hu\*

All-solid-state rechargeable sodium (Na)-ion batteries are promising for inexpensive and high-energy-density large-scale energy storage. In this contribution, new Na solid electrolytes,  $\text{Na}_{3-y}\text{PS}_{4-x}\text{Cl}_x$ , are synthesized with a strategic approach, which allows maximum substitution of Cl for S ( $x = 0.2$ ) without significant compromise of structural integrity or Na deficiency. A maximum conductivity of  $1.96 \text{ mS cm}^{-1}$  at  $25^\circ\text{C}$  is achieved for  $\text{Na}_{3.0}\text{PS}_{3.8}\text{Cl}_{0.2}$ , which is two orders of magnitude higher compared with that of tetragonal  $\text{Na}_3\text{PS}_4$  (t- $\text{Na}_3\text{PS}_4$ ). The activation energy ( $E_a$ ) is determined to be  $0.19 \text{ eV}$ . Ab initio molecular dynamics simulations shed light on the merit of maximizing Cl-doping while maintaining low Na deficiency in enhanced Na-ion conduction. Solid-state nuclear magnetic resonance (NMR) characterizations confirm the successful substitution of Cl for S and the resulting change of P oxidation state from  $5+$  to  $4+$ , which is also verified by spin moment analysis. Ion transport pathways are determined with a tracer-exchange NMR method. The functional defects that promote Na-ion transport are maximized for further improvement in ionic conductivity. Full-cell performance is demonstrated using  $\text{Na}/\text{Na}_{3.0}\text{PS}_{3.8}\text{Cl}_{0.2}/\text{Na}_3\text{V}_2(\text{PO}_4)_3$  with a reversible capacity of  $\approx 100 \text{ mAh g}^{-1}$  at room temperature.

applications.<sup>[1–3]</sup> Solid-state rechargeable batteries, owing to their potential of higher energy density, improved safety, and simplified fabrication process compared with current liquid-based electrolytes, are considered as the next-generation solutions for electrochemical energy storage. Solid electrolytes with fast Na-ion conduction, compatibility with electrodes, processability, and good mechanical properties<sup>[4]</sup> are essential to the development of high-performance solid-state rechargeable sodium-ion batteries.

Na solid electrolytes have been commercialized in high-temperature sodium-sulfur batteries using sintered  $\beta''$ -alumina.<sup>[5]</sup> However, the cell operation requires high temperatures above  $300^\circ\text{C}$  which presents several disadvantages in safety, corrosion, and additional power consumption. Na oxide ion conductors such as NASICON electrolytes<sup>[6–8]</sup> exhibit high ionic conductivities over  $1 \text{ mS cm}^{-1}$  at room temperature, but their synthesis often necessitates

high temperatures of  $>1100^\circ\text{C}$  to reduce grain-boundary resistance. The high sintering temperature and existence of grain boundaries liable for dendrite formation limit their practical applications. In addition, their chemical, electrochemical, and mechanical stability is another challenge to address.

Thiophosphate-based Na-ion conductors with enhanced processability can be incorporated into solid-state batteries with cold press. They can be synthesized at much lower temperatures and often show higher ionic conductivities, compared to Na oxide ion conductors.

The cubic phase of  $\text{Na}_3\text{PS}_4$  (c- $\text{Na}_3\text{PS}_4$ , an analogue of  $\text{Li}_3\text{PS}_4$ ) from the  $\text{Na}_2\text{S-P}_2\text{S}_5$  system was first reported by Hayashi et al. in 2012 with a measured  $\text{Na}^+$  conductivity of  $0.2 \text{ mS cm}^{-1}$ .<sup>[9]</sup> Further improvement in ionic conductivity has been achieved by Si doping ( $0.74 \text{ mS cm}^{-1}$ ).<sup>[3,10]</sup> Furthermore, substitution of S with larger Se ions increased the ionic conductivity to  $1.16 \text{ mS cm}^{-1}$  and replacement of P with As increased the conductivity to  $1.46 \text{ mS cm}^{-1}$  though at the expense of reduced electrochemical stability.<sup>[1,11,12]</sup> The tetragonal- $\text{Na}_3\text{PS}_4$  (t- $\text{Na}_3\text{PS}_4$ ) phase has a low ionic conductivity of  $0.05 \text{ mS cm}^{-1}$ ,<sup>[13]</sup> which can be significantly improved to reach  $\approx 1.1 \text{ mS cm}^{-1}$  by creating structural defects with Cl doping.<sup>[14]</sup> In addition, halogen

## 1. Introduction


Sodium (Na)-ion rechargeable batteries, which utilize abundant Na as charge carriers, are an inexpensive alternative to lithium-ion batteries, especially for large-scale energy storage

Dr. X. Feng, P.-H. Chien, P. Wang, M. Immediato-Scuotto, H. Arabzadeh, Prof. Y.-Y. Hu

Department of Chemistry and Biochemistry  
Florida State University  
95 Chieftan Way, Tallahassee, FL 32306, USA

Z. Zhu, Dr. I.-H. Chu, Prof. S. P. Ong  
Department of NanoEngineering  
University of California San Diego  
9500 Gilman Drive, La Jolla, CA 92093-0448, USA

Prof. Y.-Y. Hu  
Center of Interdisciplinary Magnetic Resonance  
National High Magnetic Field Laboratory  
1800 East Paul Dirac Drive, Tallahassee, FL 32310, USA  
E-mail: hu@chem.fsu.edu

 The ORCID identification number(s) for the author(s) of this article can be found under <https://doi.org/10.1002/adfm.201807951>.

DOI: 10.1002/adfm.201807951

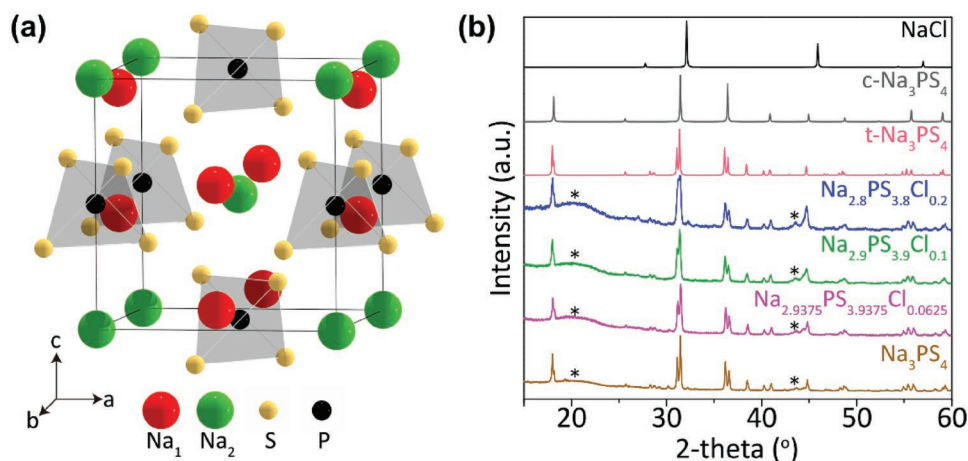


**Figure 1.** Structure and powder X-ray diffraction characterizations of  $t\text{-Na}_{3-x}\text{PS}_{4-x}\text{Cl}_x$ . a) Crystal structure of pristine tetragonal- $\text{Na}_3\text{PS}_4$  (space group =  $P-42_1c$ ). Two crystallographically distinct sites  $\text{Na}_1$  (4d) and  $\text{Na}_2$  (2a), are shown in green and red, respectively. b) Powder X-ray diffraction patterns of  $t\text{-Na}_{3-x}\text{PS}_{4-x}\text{Cl}_x$  ( $x = 0, 0.0625, 0.1, \text{ and } 0.2$ ). Asterisk (\*) indicates the background signals from sample holder and Kapton film.

doping promotes the formation of passivating solid-electrolyte interphases, which significantly improves the interfacial stability of thiophosphate-based solid electrolytes when used in all-solid-state batteries.<sup>[14]</sup>

In the typical halogen-doped  $\text{Na}_3\text{PS}_4$  compounds, halide doping for  $\text{S}^{2-}$  is charge compensated by Na vacancies, that is,  $\text{Na}_{3-x}\text{PS}_{4-x}\text{Cl}_x$ . However, the resulting Na deficiency can decrease both the ionic charge carrier concentration and the volume of Na conduction channel, which contributes negatively to the improvement of ionic conductivity. Herein, we report a new synthesis strategy to enhance the ionic conductivity of modified  $t\text{-Na}_3\text{PS}_4$ . This new strategy is informed by the identification of the functional defects that promote fast ion conduction through understanding the ion transport mechanism. The synthesis approach is designed to maximize those functional defects and minimize detrimental ones to fast ion conduction.

In the following, we start by presenting the strategic synthesis of fast Na-ion conductors with a room-temperature ionic conductivity of  $1.96 \text{ mS cm}^{-1}$  and an activation energy of  $0.19 \text{ eV}$  ( $\text{Na}_{3.0}\text{PS}_{3.8}\text{Cl}_{0.2}$ ). Then the Na-ion conduction mechanism is explained based on the results of tracer-exchange nuclear magnetic resonance (NMR) with a discussion of the structure-ion conduction correlation and the rationale for the strategic synthesis. We provide evidence from density functional theory (DFT) calculations that independent tuning of Cl doping and Na deficiency helps boosting the  $\text{Na}^+$  conductivity. The conversion of  $\text{P}^{5+}$  to  $\text{P}^{4+}$  is also observed from both solid-state  $^{31}\text{P}$  NMR peak shifting and integrated polarized-spin charge density calculations. The manuscript concludes with a performance demonstration of the new Na solid electrolyte within a full solid-state rechargeable Na-ion battery.

## 2. Results and Discussions

### 2.1. Synthesis and Structural Characterizations of $t\text{-Na}_{3-x}\text{PS}_{4-x}\text{Cl}_x$

Two crystal structures of  $\text{Na}_3\text{PS}_4$  have been reported, tetragonal- and cubic phase.<sup>[9,13,14]</sup>  $c\text{-Na}_3\text{PS}_4$  adopts the space group

of  $I-43m$  with the lattice parameter  $a = 6.9965 \text{ \AA}$ . while  $t\text{-Na}_3\text{PS}_4$  crystallizes in  $P-42_1c$  with lattice parameters of  $a = 6.9520 \text{ \AA}$  and  $c = 7.0757 \text{ \AA}$ . These two forms are significantly different in Na positions: in  $c\text{-Na}_3\text{PS}_4$ , Na is reported to occupy the 12d site while in  $t\text{-Na}_3\text{PS}_4$ , Na sits at both 2a and 4d sites. Na-ion conductivity is reported to be on the order of  $10^{-4} \text{ S cm}^{-1}$  for glass-ceramic  $c\text{-Na}_3\text{PS}_4$ ,<sup>[9]</sup> but this value is much smaller for glass-ceramic  $t\text{-Na}_3\text{PS}_4$ ,  $10^{-5} \text{ S cm}^{-1}$ .<sup>[13,14]</sup> The goal of this study is to understand how different structural defects affect Na-ion conduction in usual Cl-doped  $t\text{-Na}_3\text{PS}_4$  ( $\text{Na}_{3-x}\text{PS}_{4-x}\text{Cl}_x$ ) and to maximize functional defects for enhancing Na-ion conduction. The insights obtained will be useful for developing other fast-ion conductors. The structure of  $t\text{-Na}_3\text{PS}_4$  is shown in **Figure 1a**, in which P is tetrahedrally coordinated with four S.  $\text{Na}_1$  and  $\text{Na}_2$  occupy 4d and 2a sites, respectively. Defects in glass-ceramic  $t\text{-Na}_3\text{PS}_4$  compounds ( $t\text{-Na}_{3-x}\text{PS}_{4-x}\text{Cl}_x$ ) are created with partial Cl replacement of S in the structure and Na deficiency is generated for charge compensation. The X-ray diffraction (XRD) patterns of  $t\text{-Na}_{3-x}\text{PS}_{4-x}\text{Cl}_x$  are shown in **Figure 1b** along with the simulated XRD patterns of  $t\text{-}$  and  $c\text{-Na}_3\text{PS}_4$ . Most of the diffraction peaks in the XRD patterns collected on  $t\text{-Na}_{3-x}\text{PS}_{4-x}\text{Cl}_x$  ( $x = 0, 0.0625, 0.1, \text{ and } 0.2$ ) come from  $t\text{-Na}_3\text{PS}_4$ , except small and broad peaks at around  $21^\circ$  and  $44^\circ$  from the Kapton film and the stainless-steel holder. The XRD patterns of  $t\text{-Na}_{3-x}\text{PS}_{4-x}\text{Cl}_x$  ( $x = 0, 0.0625, 0.1, \text{ and } 0.2$ ) only exhibit very slight difference, and the most visible one is the merging of the two diffraction peaks at  $2\theta = 30.79^\circ$  and  $31.09^\circ$ . This may suggest the exchange of the two Na sites in  $t\text{-Na}_3\text{PS}_4$ , which makes the structure gradually converge to  $c\text{-Na}_3\text{PS}_4$  with increasing  $x$ . In addition, some minor peaks from impurities appear in the case of  $\text{Na}_{2.8}\text{PS}_{3.8}\text{Cl}_{0.2}$ , which is consistent with calculation results.<sup>[14]</sup> The thermal stability is greatly compromised with increased  $x$  value in  $t\text{-Na}_{3-x}\text{PS}_{4-x}\text{Cl}_x$ .

### 2.2. $\text{Na}^+$ Conduction in $t\text{-Na}_{3-x}\text{PS}_{4-x}\text{Cl}_x$

The ionic conductivity of  $t\text{-Na}_{3-x}\text{PS}_{4-x}\text{Cl}_x$  ( $x = 0, 0.0625, 0.1, \text{ and } 0.2$ ) samples is determined with electrochemical impedance

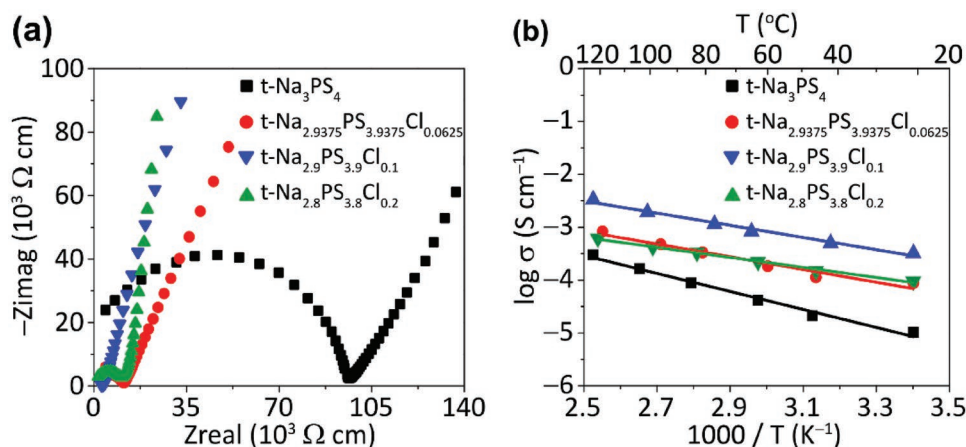


**Figure 2.** Electrochemical impedance measurements at 21 °C and ionic conductivities of  $t\text{-Na}_{3-x}\text{PS}_{4-x}\text{Cl}_x$ . a) Nyquist plots of  $t\text{-Na}_{3-x}\text{PS}_{4-x}\text{Cl}_x$  ( $x = 0, 0.0625, 0.1, \text{ and } 0.2$ ). b) Arrhenius plots of  $t\text{-Na}_{3-x}\text{PS}_{4-x}\text{Cl}_x$  ( $x = 0, 0.0625, 0.1, \text{ and } 0.2$ ).

spectroscopy (EIS) and the results are shown in **Figure 2a**. The ionic conductivity of  $t\text{-Na}_3\text{PS}_4$  is  $\approx 10^{-5} \text{ S cm}^{-1}$  at room temperature (Figure 2), compared with  $\approx 10^{-4} \text{ S cm}^{-1}$  for  $c\text{-Na}_3\text{PS}_4$ .<sup>[9]</sup> Cl replacement of S in  $t\text{-Na}_{3-x}\text{PS}_{4-x}\text{Cl}_x$  leads to significantly improved Na-ion conduction. The highest conductivity of  $0.3 \text{ mS cm}^{-1}$  at room temperature is obtained when  $x$  equals 0.1, that is,  $t\text{-Na}_{2.9}\text{PS}_{3.9}\text{Cl}_{0.1}$ . Larger or smaller  $x$  values yield larger impedance and thus slower ion conduction (Figure 2a).

The ionic conductivities of  $t\text{-Na}_{3-x}\text{PS}_{4-x}\text{Cl}_x$  are also measured at variable temperatures within the range of 21–120 °C (Figure S2, Supporting Information) and the results are shown in Figure 2b. The activation energy,  $E_a$ , is determined based on the Arrhenius equation

$$\sigma = A \times \exp\left(\frac{-E_a}{RT}\right) \quad (1)$$

where  $A$  is a constant,  $R$  is the universal gas constant with the value of  $8.314 \times 10^{-3} \text{ kJ mol}^{-1} \text{ K}^{-1}$ , and  $T$  is temperature in Kelvin. The activation energy of  $t\text{-Na}_3\text{PS}_4$  is determined to be 0.34 eV, and it decreases with more Cl  $\rightarrow$  S replacement (0.24 eV for  $\text{Na}_{2.9375}\text{PS}_{3.9375}\text{Cl}_{0.0625}$ , 0.23 eV for  $\text{Na}_{2.9}\text{PS}_{3.9}\text{Cl}_{0.1}$ , and 0.19 eV for  $\text{Na}_{2.8}\text{PS}_{3.8}\text{Cl}_{0.2}$ ). As a reference, the activation energy for most solid electrolytes is  $>0.24 \text{ eV}$ .<sup>[2,14,15]</sup> The achieved small activation energy in  $t\text{-Na}_{3-x}\text{PS}_{4-x}\text{Cl}_x$  is beneficial for flexible adaption of these solid electrolytes to be used in different climates especially at low temperatures with no significant decrease in ionic conductivity.

### 2.3. Solid-State $^{23}\text{Na}$ NMR Characterizations of Structural Defects

To identify structural features that contribute to Na-ion conduction in  $t\text{-Na}_{3-x}\text{PS}_{4-x}\text{Cl}_x$  ( $x = 0, 0.0625, 0.1, \text{ and } 0.2$ ), high-resolution solid-state magic-angle-spinning (MAS)  $^{23}\text{Na}$  NMR in a high magnetic field of 19.6 T is employed for identifying the local structural environments of Na ions and then tracer-exchange NMR is used to probe Na-ion transport pathways. As shown in **Figure 3**, a clear evolution of  $^{23}\text{Na}$  resonances

is observed as  $x$  increases in  $t\text{-Na}_{3-x}\text{PS}_{4-x}\text{Cl}_x$ . The  $^{23}\text{Na}$  spectrum of  $t\text{-Na}_3\text{PS}_4$  shows two main resonance peaks at 3.1 and 3.4 ppm, and the corresponding quadrupolar coupling constants  $C_Q$  are 1.7 and 2.3 MHz (see the Supporting Information). These are assigned to  $\text{Na}_1$  and  $\text{Na}_2$  sites in the  $t\text{-Na}_3\text{PS}_4$  structure. Large  $C_Q$  values for  $\text{Na}_1$  and  $\text{Na}_2$  resonances suggest an asymmetric structural environment with low Na mobility. In addition to  $\text{Na}_1$  and  $\text{Na}_2$  resonances, another NMR component appears at 12 ppm with a  $C_Q$  value of 2.4 MHz (marked with #). This accounts for 4.5% of the total  $^{23}\text{Na}$  integral and may come from defective sites. Upon partial replacement of S by Cl in  $t\text{-Na}_{3-x}\text{PS}_{4-x}\text{Cl}_x$ , two new resonances labeled as  $\text{Na}_3$  and  $\text{Na}_4$  emerge at 9.6 and 18 ppm with vanished quadrupolar interactions,  $C_Q = 0$ . These two  $^{23}\text{Na}$  resonances arise from defective structural sites introduced by the Cl  $\rightarrow$  S replacement, and the amount of these defects increases with the  $x$  values in  $t\text{-Na}_{3-x}\text{PS}_{4-x}\text{Cl}_x$  (Figure 3). In principle, the  $C_Q$  values should increase for nonsymmetric defective sites. The obtained small  $C_Q$ 's for  $\text{Na}_3$  and  $\text{Na}_4$  suggest fast Na-ion motion, which significantly reduces quadrupolar coupling interactions of  $^{23}\text{Na}$  spins. Another evidence of fast Na-ion motion is the significantly larger  $T_1$  relaxation times for  $\text{Na}_3$  sites ( $\approx 10 \text{ s}$ ) compared with those for  $\text{Na}_1$  and  $\text{Na}_2$  sites ( $< \approx 0.2 \text{ s}$ ) in  $t\text{-Na}_3\text{PS}_4$  (see the Supporting Information). For  $\text{Na}_1$  and  $\text{Na}_2$ , the  $^{23}\text{Na}$  NMR  $T_1$  relaxation is driven by quadrupolar interactions and the relaxation time is typically on the order of milliseconds, while for  $\text{Na}_3$  and  $\text{Na}_4$ , with the quadrupolar interactions minimized by fast Na motion, the NMR relaxation is driven by other interactions such as dipolar couplings and the typical  $T_1$  relaxation time is on the order of seconds.  $\text{Na}_3$  is assigned to Na sites close to Cl and  $\text{Na}_4$  to Na sites in the vicinity of Na vacancies, based on the fact that  $\text{Na}_4$  resonance is reduced as the Na vacancies are filled, as discussed later in this work.

### 2.4. Na-Ion Transport Mechanism in $t\text{-Na}_{2.8}\text{PS}_{3.8}\text{Cl}_{0.2}$

To understand how the structural defects generated by Cl  $\rightarrow$  S replacement contribute to the significantly improved ionic conductivity in  $t\text{-Na}_{3-x}\text{PS}_{4-x}\text{Cl}_x$ , tracer-exchange NMR<sup>[16]</sup> is employed

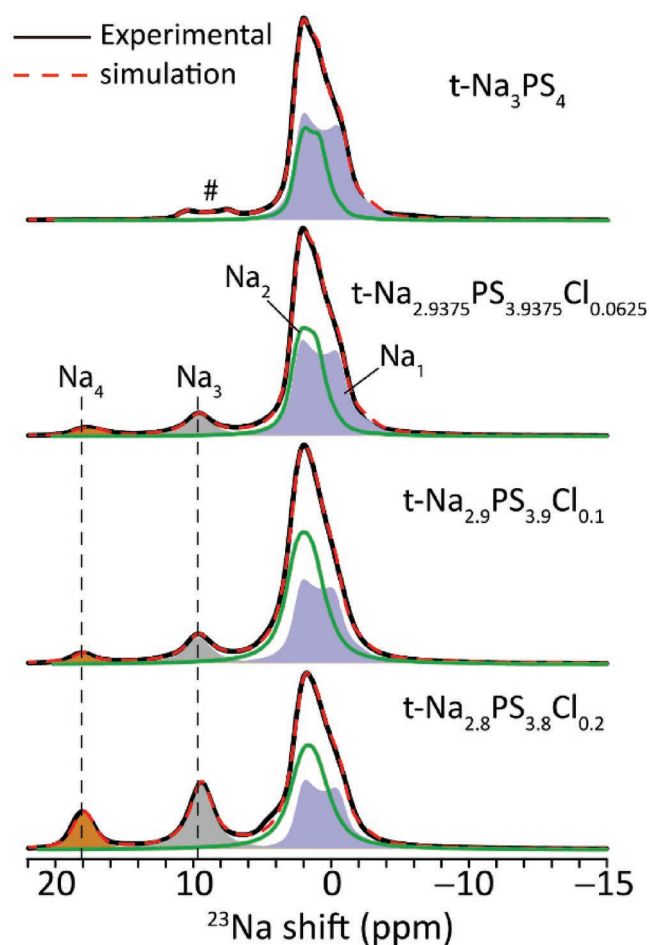


**Figure 3.** Evolution of structural defects in  $t\text{-Na}_{3-x}\text{PS}_{4-x}\text{Cl}_x$  ( $x = 0, 0.0625, 0.1, \text{ and } 0.2$ ) electrolytes probed by  $^{23}\text{Na}$  solid-state magic-angle-spinning (MAS) NMR.  $^{23}\text{Na}$  MAS NMR spectra together with simulation results of  $t\text{-Na}_{3-x}\text{PS}_{4-x}\text{Cl}_x$  ( $x = 0, 0.0625, 0.1, \text{ and } 0.2$ ).

to probe Na-ion transport pathways in  $t\text{-Na}_{3-x}\text{PS}_{4-x}\text{Cl}_x$ . Ideally, these experiments should be carried out by monitoring the replacement of one Na isotope with another under relevant electrochemical condition. However, as Na has only one isotope, that is,  $^{23}\text{Na}$ , an alternative strategy is adopted by using Li to replace Na driven by a biased electric potential. In the experimental setup, the  $t\text{-Na}_{3-x}\text{PS}_{4-x}\text{Cl}_x$  solid electrolyte pellet is sandwiched by two pieces of  $^7\text{Li}$  metal (Figure 4a). Driven by a biased potential, Li ions diffuse through the solid electrolyte and on the pathway, Li ions replace active Na ions. By identifying at which structural sites Na ions are replaced, the ion transport pathways can be identified. This tracer-exchange experiment is performed on  $t\text{-Na}_{2.8}\text{PS}_{3.8}\text{Cl}_{0.2}$  and the results are shown in Figure 4b,c. Significant decrease in the intensity of the  $\text{Na}_3$  and  $\text{Na}_4$  resonances after tracer exchange and increase in  $\text{Na}_1$  and  $\text{Na}_2$  resonances are observed. The decrease in  $\text{Na}_4$  resonance intensity and increase in  $\text{Na}_1$  and  $\text{Na}_2$  amount are correlated. Li fills Na vacancies in  $t\text{-Na}_{2.8}\text{PS}_{3.8}\text{Cl}_{0.2}$ , which leads to the conversion of Na sites next to Na vacancies, that is,  $\text{Na}_4$  to  $\text{Na}_1$  and  $\text{Na}_2$ . The decrease in  $\text{Na}_3$  amount is due to the replacement of  $^{23}\text{Na}$  by  $^7\text{Li}$ . The results suggest that  $\text{Na}_3$ , which is Na next to Cl, is the active site for ion conduction. This

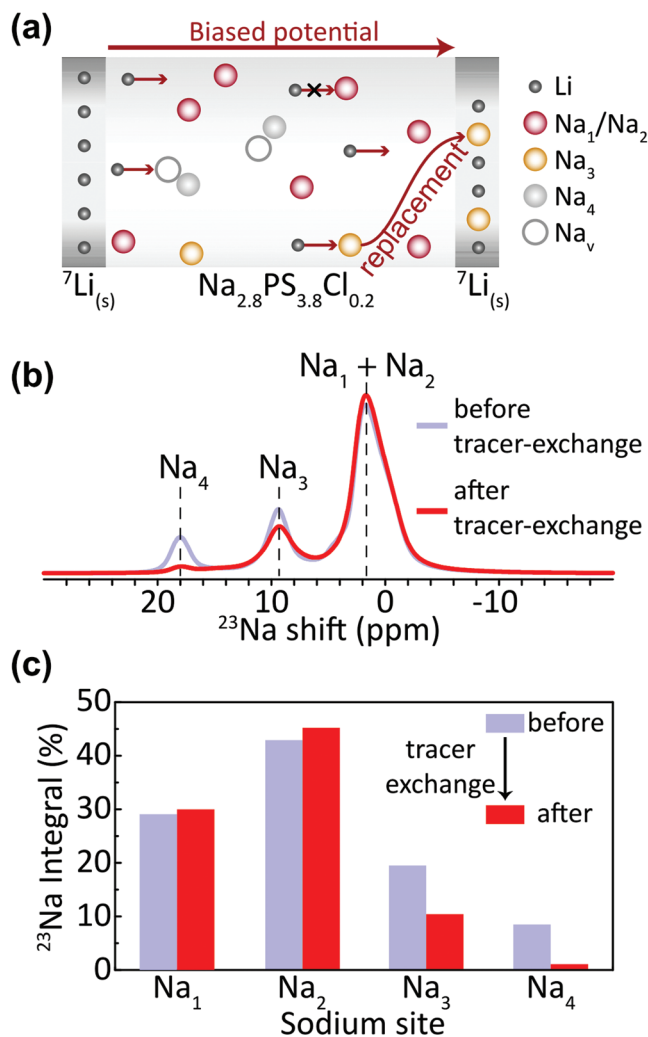


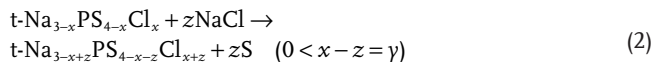
**Figure 4.** Identification of functional defects with tracer-exchange NMR and  $^{23}\text{Na}$  solid-state MAS NMR. a) Schematic of electrochemically driven  $^7\text{Li} \rightarrow ^{23}\text{Na}$  tracer-exchange method. b)  $^{23}\text{Na}$  MAS NMR spectra and c) quantification of  $t\text{-Na}_{2.8}\text{PS}_{3.8}\text{Cl}_{0.2}$  before/after  $^7\text{Li} \rightarrow ^{23}\text{Na}$  tracer exchange.

is also confirmed by the positive correlation of enhanced ionic conductivity and the amount of  $\text{Na}_3$  in  $t\text{-Na}_{2.8}\text{PS}_{3.8}\text{Cl}_{0.2}$ . On the other hand, the amount of Na vacancy concentration seems to correlate negatively with the increase in ionic conductivity at higher concentration.

Tracer-exchange NMR provides chemical-specific information on ion transport pathways, identifying the new  $\text{Na}_3$  sites as the key for significantly enhanced ion conduction. The 3D diffusion pathways can be visualized from  $\text{Na}^+$  probability density distribution (see Figure S7, Supporting Information). In  $t\text{-Na}_{2.9375}\text{PS}_{3.875}\text{Cl}_{0.125}$ , 3D diffusion pathways comprise chains of  $\text{Na}_1$  sites along the  $c$ -direction and highly cooperative  $\text{Na}_1\text{-Na}_2\text{-Na}_1$  (including those sites converted to  $\text{Na}_3$ ) hopping within  $ab$ -plane, which form the cubic sublattice, similar to that observed in previous studies of Cl-doped  $\text{Na}_3\text{PS}_4$ .<sup>[14]</sup>

Based on the understanding of ion transport mechanism in  $t\text{-Na}_{2.8}\text{PS}_{3.8}\text{Cl}_{0.2}$ , to further enhance the ionic conductivity, the amount of  $\text{Na}_3$  needs to be increased while Na vacancies

should be minimized, which means large  $x$  and small  $y$  in  $t\text{-Na}_{3-y}\text{PS}_{4-x}\text{Cl}_x$ . New synthesis strategies are needed to maximize the  $\text{Cl} \rightarrow \text{S}$  replacement while preventing significant Na vacancy formation. Following this guideline, we have designed the following reaction to synthesize  $t\text{-Na}_{3-y}\text{PS}_{4-x}\text{Cl}_x$  with improved ionic conductivity



Vacuum is applied to remove the product S during the synthesis, which drives the reaction to proceed to the right. With this method, several compounds are synthesized starting with  $t\text{-Na}_{2.9}\text{PS}_{3.9}\text{Cl}_{0.1}$  and  $t\text{-Na}_{2.8}\text{PS}_{3.8}\text{Cl}_{0.2}$ . The results for  $t\text{-Na}_{2.9}\text{PS}_{3.9}\text{Cl}_{0.1}/z\text{NaCl}$  series are presented in the following with the corresponding data for the  $t\text{-Na}_{2.8}\text{PS}_{3.8}\text{Cl}_{0.2}/z\text{NaCl}$  series shown in Figures S3, S4, S5 and S6 (Supporting Information).

The XRD patterns of the  $t\text{-Na}_{2.9}\text{PS}_{3.9}\text{Cl}_{0.1}/z\text{NaCl}$  ( $z = 0.1, 0.3$ , and  $0.5$ ) series are shown in Figure 5a along with the reference patterns of  $t\text{-Na}_3\text{PS}_4$  and NaCl. The incorporation of 0.1 NaCl to  $t\text{-Na}_{2.9}\text{PS}_{3.9}\text{Cl}_{0.1}$  is successful, manifested as no observed NaCl diffraction peaks. Also, the additional NaCl modifies the  $t\text{-Na}_{2.9}\text{PS}_{3.9}\text{Cl}_{0.1}$  structure to converge to the cubic structure, suggested by the merging of the diffraction peaks at  $2\theta = 30.79^\circ$  and  $31.09^\circ$ . When 0.3 NaCl is added to  $t\text{-Na}_{2.9}\text{PS}_{3.9}\text{Cl}_{0.1}$ , minor NaCl residues are seen from the XRD pattern and the NaCl peaks become obvious with 0.5 NaCl added. To further probe the structural changes induced by the added NaCl, high-resolution  $^{23}\text{Na}$  NMR spectra are acquired and presented in Figure 5b. As expected, the addition of 0.1 NaCl to  $t\text{-Na}_{2.9}\text{PS}_{3.9}\text{Cl}_{0.1}$  fills the Na vacancies, thus the disappearance of the 18 ppm resonance ( $\text{Na}_4$ ). When more NaCl is added, the resonance from NaCl at 6.6 ppm arises and increases. Summarizing the results from both PXRD and NMR, the  $z$  value in  $t\text{-Na}_{2.9}\text{PS}_{3.9}\text{Cl}_{0.1}/z\text{NaCl}$  should be less than 0.1 to achieve the goal of filling Na vacancies without introducing NaCl impurity. The real formula of  $t\text{-Na}_{2.9}\text{PS}_{3.9}\text{Cl}_{0.1}/0.1\text{NaCl}$  should be  $t\text{-Na}_{3.0}\text{PS}_{3.8}\text{Cl}_{0.2}$ , based on the XRD and NMR results. The optimal  $z$ -value in  $t\text{-Na}_{2.8}\text{PS}_{3.8}\text{Cl}_{0.2}/z\text{NaCl}$  is determined to be 0.2 (Figure S6,

Supporting Information) and the formula for the best sample should be  $t\text{-Na}_{3.0}\text{PS}_{3.6}\text{Cl}_{0.4}$ .

## 2.5. Enhanced Na-Ion Conduction with Maximizing Functional Defects in $t\text{-Na}_{3-y}\text{PS}_{4-x}\text{Cl}_x$

As suggested by tracer-exchange NMR,  $\text{Na}_3$  site is responsible for Na conduction. Therefore, Na ionic conductivity can be increased by maximizing  $\text{Cl} \rightarrow \text{S}$  replacement and minimizing Na vacancy formation ( $\text{Na}_4$ ). Figure 6 presents the results of AC impedance measurements on several  $t\text{-Na}_{2.9}\text{PS}_{3.9}\text{Cl}_{0.1}/z\text{NaCl}$  ( $z = 0.1, 0.3$ , and  $0.5$ ) compounds to validate the hypothesis. By filling Na vacancies in  $t\text{-Na}_{2.9}\text{PS}_{3.9}\text{Cl}_{0.1}/z\text{NaCl}$  ( $z = 0.1, 0.3$ , and  $0.5$ ), the ionic conductivity is increased. The highest ionic conductivity ( $1.77 \text{ mS cm}^{-1}$  at  $21^\circ\text{C}$  and  $1.96 \text{ mS cm}^{-1}$  at  $25^\circ\text{C}$ ) is obtained for  $t\text{-Na}_{2.9}\text{PS}_{3.9}\text{Cl}_{0.1}/0.1\text{NaCl}$ , nominally  $t\text{-Na}_{3.0}\text{PS}_{3.8}\text{Cl}_{0.2}$ . For  $z = 0.3$  and  $0.5$ , an impurity of NaCl is produced and the observed ionic conductivity is slightly lowered. The activation energy for Na-ion conduction in  $t\text{-Na}_{3.0}\text{PS}_{3.8}\text{Cl}_{0.2}$  is determined to be 0.19 eV with variable temperature EIS (Figure 6b).

Ab initio molecular dynamics (AIMD) simulations are performed to verify the doping effect of Cl and Na vacancy in  $t\text{-Na}_{3-y}\text{PS}_{4-x}\text{Cl}_x$  ( $x = 0.0625$  and  $0.125$ ;  $y = 0, 0.0625$ , and  $0.125$ ) on Na ionic conductivity. The calculated Arrhenius plots for structures with various Cl doping/Na vacancy ratio are shown in Figure 7. The conductivity of pristine  $t\text{-Na}_3\text{PS}_4$  is poor ( $<0.01 \text{ mS cm}^{-1}$ ) but can be increased to  $1.38 \text{ mS cm}^{-1}$  by introducing 2.1% Na vacancy, as reported in previous work.<sup>[14]</sup> When Cl concentration increases, we find that the conductivity of  $t\text{-Na}_{2.875}\text{PS}_{3.875}\text{Cl}_{0.125}$  can be pushed to a higher value of  $6.38 \text{ mS cm}^{-1}$ , with low activation energy of 0.199 eV. When Na vacancies are partially filled while maintaining the Cl concentration ( $\text{Na}_{2.9375}\text{PS}_{3.875}\text{Cl}_{0.125}$ ), the conductivity is further increased to  $9.03 \text{ mS cm}^{-1}$  and the activation energy is reduced to 0.174 eV, which is consistent with the experimental results. However, the conductivity decreases sharply to close to that of pristine  $t\text{-Na}_3\text{PS}_4$  when all Na vacancies are filled ( $\text{Na}_3\text{PS}_{4-x}\text{Cl}_x$ ,

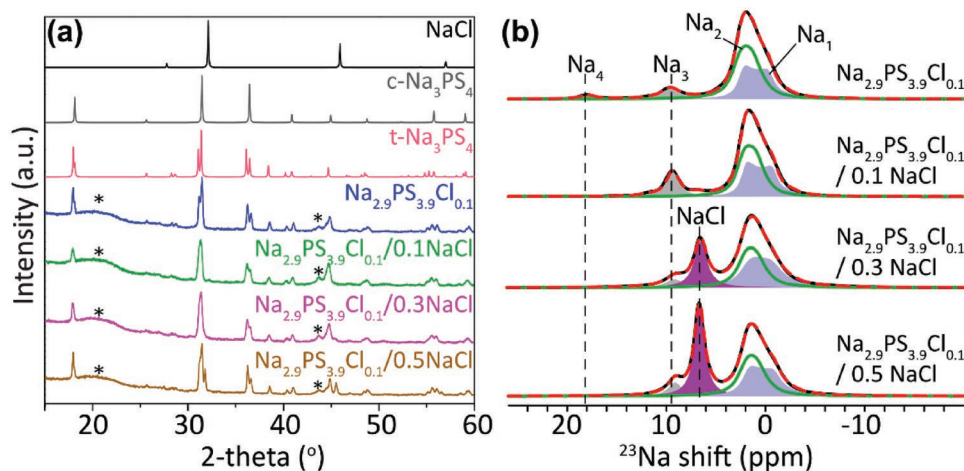


**Figure 5.** Structure characterizations of synthesized  $t\text{-Na}_{2.9}\text{PS}_{3.9}\text{Cl}_{0.1}/z\text{NaCl}$  ( $z = 0, 0.1, 0.3$ , and  $0.5$ ). a) Powder X-ray diffraction patterns and b)  $^{23}\text{Na}$  MAS NMR spectra of  $t\text{-Na}_{2.9}\text{PS}_{3.9}\text{Cl}_{0.1}/z\text{NaCl}$  ( $z = 0, 0.1, 0.3$ , and  $0.5$ ). Asterisk (\*) indicates the background signals from sample holder and polyimide film.

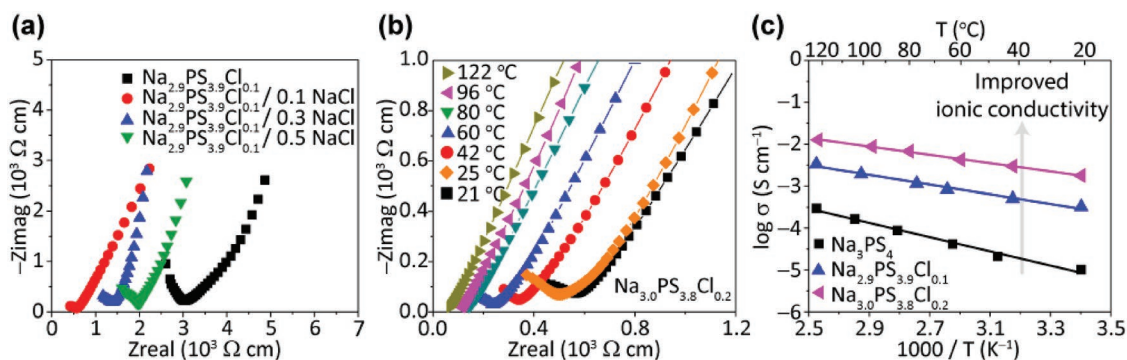


**Figure 6.** Enhanced ionic conductivities of  $t\text{-Na}_{3-y}\text{PS}_{4-x}\text{Cl}_x$ . a) Nyquist plots of  $t\text{-Na}_{2.9}\text{PS}_{3.9}\text{Cl}_{0.1}/z\text{NaCl}$  ( $z = 0, 0.1, 0.3$ , and  $0.5$ ). b) Variable-temperature impedance spectra of  $t\text{-Na}_{2.9}\text{PS}_{3.9}\text{Cl}_{0.1}/0.1\text{NaCl}$ . c) Arrhenius plots of  $t\text{-Na}_3\text{PS}_4$ ,  $t\text{-Na}_{2.9}\text{PS}_{3.9}\text{Cl}_{0.1}$ , and  $t\text{-Na}_{2.9}\text{PS}_{3.9}\text{Cl}_{0.1}/0.1\text{NaCl}$ .

$x = 0.0625$  and  $0.125$ ). It should be noted that  $^{23}\text{Na}$  NMR studies show no sign of Na vacancies for the  $\text{Na}_{3.0}\text{PS}_{3.8}\text{Cl}_{0.2}$  nor  $\text{Na}_{3.0}\text{PS}_{3.6}\text{Cl}_{0.4}$  which exhibit highest ionic conductivities of all the  $t\text{-Na}_{3-y}\text{PS}_{4-x}\text{Cl}_x$  compounds synthesized in this work. This discrepancy is likely due to amount of Na vacancies is too small to be detected. As shown in Figure 3, in  $\text{Na}_{2.9375}\text{PS}_{3.9375}\text{Cl}_{0.0625}$ ,  $\text{Na}_4$  resonance which represents Na vacancies can be clearly observed. The estimated detection limit of Na vacancies should be much smaller than  $0.0625/3 \approx 2\%$ .

Topological analyses using open source software<sup>[17]</sup> Zeo++ are conducted to assess the free channel volumes for structures with different Cl dopant/Na vacancy ratio. As shown in Table S5 (Supporting Information), when the Na vacancy is fixed, for example,  $\text{Na}_{2.9375}\text{PS}_{3.9375}\text{Cl}_{0.0625}$  versus  $\text{Na}_{2.9375}\text{PS}_{3.875}\text{Cl}_{0.125}$ , the introduction of Cl dopants leads to larger Na channel volumes. In contrast, Na vacancies lead to a decrease in channel volumes. For example, a 2.1% Na vacancy concentration decreases the channel volume from 937 to 924 Å<sup>3</sup>. From a series of AIMD results, we find that in the presence of small amount of Na vacancy, increase of Cl doping concentration significantly improves the Na<sup>+</sup> conductivity. The calculated channel volume and conductivity results indicate

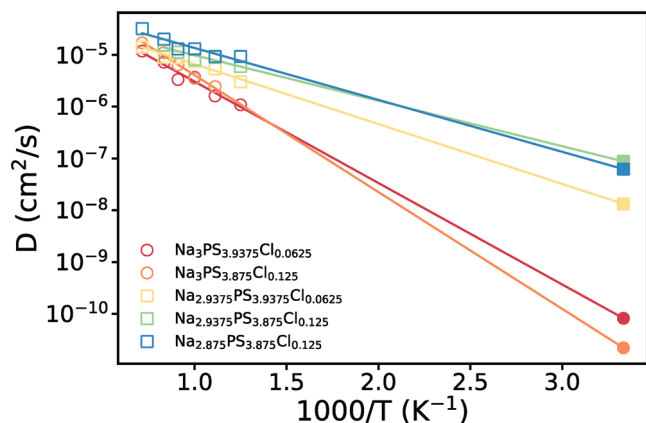


**Figure 7.** Ionic diffusivity of  $t\text{-Na}_{3-y}\text{PS}_{4-x}\text{Cl}_x$  from AIMD simulations. Arrhenius plots for  $\text{Na}_3\text{PS}_{3.9375}\text{Cl}_{0.0625}$  (red),  $\text{Na}_3\text{PS}_{3.875}\text{Cl}_{0.125}$  (orange),  $\text{Na}_{2.9375}\text{PS}_{3.9375}\text{Cl}_{0.0625}$  (yellow),  $\text{Na}_{2.9375}\text{PS}_{3.875}\text{Cl}_{0.125}$  (green), and  $\text{Na}_{2.875}\text{PS}_{3.875}\text{Cl}_{0.125}$  (blue) obtained from AIMD simulations. Squares and circles denote compositions with and without Na vacancies, respectively. Filled circles or squares indicate the extrapolated diffusivities at 300 K.

that independent tuning of Cl and Na vacancy amount can lead to optimized conduction performance. Without compensating Na vacancies, the introduction of the Cl<sup>-</sup> dopant is charge compensated by the reduction of P, as shown in the next section.

## 2.6. Change of P Oxidation State in $t\text{-Na}_{3-y}\text{PS}_{4-x}\text{Cl}_x$

Cl → S replacement also leads to changes in the local structural environment of P as seen in <sup>31</sup>P NMR (Figure S8, Supporting Information). In addition to <sup>31</sup>P resonances from  $t\text{-Na}_3\text{PS}_4$  at  $\approx 87$  ppm, additional <sup>31</sup>P NMR peaks appear between 105 and 115 ppm for  $t\text{-Na}_{3-y}\text{PS}_{4-x}\text{Cl}_x$ . P with an oxidation state of 4+ often resonates at a position >100 ppm, for instance, P in  $\text{Li}_4\text{P}_2\text{S}_6$  ( $\text{Li}_2\text{PS}_3$ ) shows multiple <sup>31</sup>P NMR peaks at >105 ppm.<sup>[18]</sup> Therefore, these additional <sup>31</sup>P resonances observed for  $t\text{-Na}_{3-y}\text{PS}_{4-x}\text{Cl}_x$  compounds suggest the conversion of P<sup>5+</sup> to P<sup>4+</sup> due to Cl → S replacement, and the amount of P<sup>4+</sup> increases with  $x$  in  $t\text{-Na}_{3-y}\text{PS}_{4-x}\text{Cl}_x$  (Figure S9, Supporting Information). Multiple <sup>31</sup>P NMR resonances at >105 ppm suggest an inhomogeneous structural environment due to Cl → S replacement. Both <sup>23</sup>Na and <sup>31</sup>P NMR indicate that Cl → S replacement in  $t\text{-Na}_{3-y}\text{PS}_{4-x}\text{Cl}_x$  does not necessarily lead to Na vacancies, instead the charge imbalance due to the replacement can at least be partially compensated by reduction of P<sup>5+</sup> to P<sup>4+</sup>. Another evidence for the formation of P<sup>4+</sup> is the formation of elemental S. We collected the powder evaporated during the synthesis of  $\text{Na}_{2.8}\text{PS}_{3.8}\text{Cl}_{0.2}$ , and characterized it using XRD. The XRD pattern of the evaporated powder highly resembles that of the standard S<sub>8</sub> (Figure S10, Supporting Information). These experimental observations are supported by plotting the spherically integrated spin-polarized charge density of all P ions as a function of cutoff radius from our DFT calculations of  $\text{Na}_3\text{PS}_{3.9375}\text{Cl}_{0.0625}$  (Figure S11, Supporting Information). A nonzero integrated spin was observed ( $\approx 1/2 \mu_B$  at the radius of 2 Å) for the P in the center of  $\text{PS}_3\text{Cl}$  tetrahedra, indicating the reduction of P<sup>5+</sup> to P<sup>4+</sup>. In contrast, all remaining P in  $\text{PS}_4$  tetrahedra has negligible net spins, that is, P<sup>5+</sup>. Besides, previous reports have suggested based on empirical evidence<sup>[19]</sup> that P<sup>4+</sup> helps to improve the stability of thiophosphate solid electrolytes.

With the formation of P<sup>4+</sup>, a concern arises that P<sup>4+</sup> can potentially serve as an electron donor, leading to enhanced electron conduction, while electron conduction is not desirable

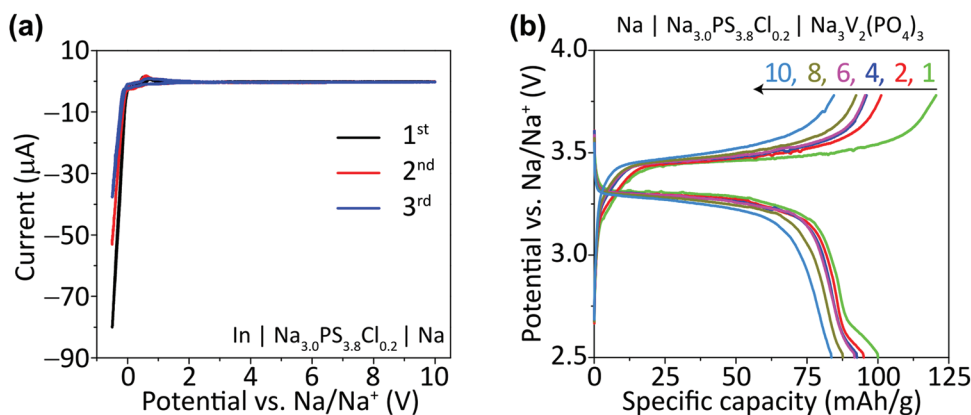


**Figure 8.** Cyclic voltammetry and electrochemical performance of a full-cell solid-state battery made of Na|t-Na<sub>3.0</sub>PS<sub>3.8</sub>Cl<sub>0.2</sub>|Na<sub>3</sub>V<sub>2</sub>(PO<sub>4</sub>)<sub>3</sub>. a) CV of a Na|t-Na<sub>3.0</sub>PS<sub>3.8</sub>Cl<sub>0.2</sub>|In cell, and b) the charge and discharge profiles of Na|t-Na<sub>3.0</sub>PS<sub>3.8</sub>Cl<sub>0.2</sub>|Na<sub>3</sub>V<sub>2</sub>(PO<sub>4</sub>)<sub>3</sub> performed at room temperature with a current density of 10 mA g<sup>-1</sup> calculated based on the mass of Na<sub>3</sub>V<sub>2</sub>(PO<sub>4</sub>)<sub>3</sub>.

for solid electrolytes. We have measured the electronic conductivity of both t-Na<sub>3</sub>PS<sub>4</sub> and t-Na<sub>3</sub>PS<sub>3.8</sub>Cl<sub>0.2</sub>, and the electronic conductivity of t-Na<sub>3</sub>PS<sub>3.8</sub>Cl<sub>0.2</sub> is  $1.2 \times 10^{-8}$  S cm<sup>-1</sup>, which is only slightly higher than that for t-Na<sub>3</sub>PS<sub>4</sub>, that is,  $0.8 \times 10^{-8}$  S cm<sup>-1</sup> (Figure S12, Supporting Information). Both values are much lower than the measured ionic conductivity  $\approx 2 \times 10^{-3}$  S cm<sup>-1</sup> for t-Na<sub>3</sub>PS<sub>3.8</sub>Cl<sub>0.2</sub>.

## 2.7. Full-Cell Performance

The stability of t-Na<sub>3-y</sub>PS<sub>4-x</sub>Cl<sub>x</sub> is tested using cyclic voltammetry within a Na|Na<sub>3.0</sub>PS<sub>3.8</sub>Cl<sub>0.2</sub>|In cell. The scan rate is 0.2 mV s<sup>-1</sup> and the battery is cycled between -0.5 and 10 V (vs Na/Na<sup>+</sup>). As seen in Figure 8a, only Na deposition and dissolution occur at around 0 V. No decomposition of Na<sub>3.0</sub>PS<sub>3.8</sub>Cl<sub>0.2</sub> is seen even at a high potential of 10 V, which is attributed to the low electronic conductivity of Na<sub>3.0</sub>PS<sub>3.8</sub>Cl<sub>0.2</sub>, limiting the rate of side reactions. The all-solid-state Na-ion battery using Na as anode, Na<sub>3.0</sub>PS<sub>3.8</sub>Cl<sub>0.2</sub> as electrolyte, and Na<sub>3</sub>V<sub>2</sub>(PO<sub>4</sub>)<sub>3</sub> as cathode achieves a capacity of 100 mAh g<sup>-1</sup> at room temperature (Figure 8b) in an initial test, with slight decay over further cycling being observed. The main cause to the capacity decay is interfacial stability upon electrochemical cycling. The impedance of the Na|Na<sub>3.0</sub>PS<sub>3.8</sub>Cl<sub>0.2</sub>|Na<sub>3</sub>V<sub>2</sub>(PO<sub>4</sub>)<sub>3</sub> full cell before and after cycling is measured and the results are shown in Figure S13 (Supporting Information). Before cycling, the total interfacial resistance is only 80 Ω and it increases to  $\approx 1300$  Ω after cycling due to nonconductive products formed at electrode-electrolyte interfaces from undesirable side reactions of Na<sub>3.0</sub>PS<sub>3.8</sub>Cl<sub>0.2</sub> with the electrodes (Na anode and Na<sub>3</sub>V<sub>2</sub>(PO<sub>4</sub>)<sub>3</sub> cathode). To improve the electrochemical performance of the full cell using Na<sub>3.0</sub>PS<sub>3.8</sub>Cl<sub>0.2</sub> as the electrolyte, Na-Sn alloy instead of Na should be employed and surface modification of cathode materials is necessary to minimize side reactions of Na<sub>3.0</sub>PS<sub>3.8</sub>Cl<sub>0.2</sub> with the cathode at high potentials.

## 3. Conclusions

A series of Cl-doped t-Na<sub>3</sub>PS<sub>4</sub> solid electrolytes have been prepared for use in all-solid-state rechargeable Na-ion batteries.

Structural analyses have been carried out with techniques including X-ray diffraction and solid-state NMR. In particular, solid-state <sup>23</sup>Na MAS NMR identifies the functional defects that promote fast ion conduction. A new synthesis strategy is implemented to maximize the fraction of functional defects while preventing the formation of other defects that impede Na-ion conduction. As a result, the best ionic conductivity is achieved in the composition of Na<sub>3</sub>PS<sub>3.8</sub>Cl<sub>0.2</sub>, which is about 170 times larger compared with t-Na<sub>3</sub>PS<sub>4</sub>, with a low activation energy of 0.19 eV. The change of P oxidation state from 5+ to 4+, which is observed from both NMR and spin moment calculations, allows the introduction of more Cl and less Na vacancy in stable structures of Na<sub>3-y</sub>PS<sub>4-x</sub>Cl<sub>x</sub>. DFT calculations verify that high ionic conductivities can be achieved by independent tuning of Na vacancy and Cl doping. The performance of Na<sub>3.0</sub>PS<sub>3.8</sub>Cl<sub>0.2</sub> is tested in a Na|Na<sub>3.0</sub>PS<sub>3.8</sub>Cl<sub>0.2</sub>|Na<sub>3</sub>V<sub>2</sub>(PO<sub>4</sub>)<sub>3</sub> cell, which delivers a capacity of 100 mAh g<sup>-1</sup>.

## 4. Experimental Section

**Synthesis of t-Na<sub>3-y</sub>PS<sub>4-x</sub>Cl<sub>x</sub> (0 ≤ y ≤ x ≤ 0.2) Solid Electrolytes:** t-Na<sub>3-y</sub>PS<sub>4-x</sub>Cl<sub>x</sub> (0 ≤ y ≤ x ≤ 0.2) solid electrolytes were prepared via solid-state reactions. All the chemicals (Na<sub>2</sub>S, P<sub>2</sub>S<sub>5</sub>, and NaCl) were purchased from Sigma-Aldrich and dried under vacuum at 120 °C overnight before use. Na<sub>2</sub>S, P<sub>2</sub>S<sub>5</sub>, and NaCl were weighed inside an Ar-filled glove box and the molar ratios were calculated based on the target compositions. The mixtures were manually ground first, then sealed in a 25 mL ZrO<sub>2</sub> jar under vacuum and ball-milled using a SPEX Sample Prep 8000M mixer for 2 h with two 10 mm ZrO<sub>2</sub> balls as the milling media. The mixtures were then cold-pressed into pellets, which were sintered at 420 °C for 12 h under vacuum with a heating rate of 1 °C min<sup>-1</sup> in a tube furnace (Carbolite MTF). The vacuum environment and temperature gradient generated within the tube furnace facilitate the extraction of S, which favors the replacement of S by Cl. Heating was then turned off to allow the sintered pellets to cool down to room temperature.

**Characterizations of t-Na<sub>3-y</sub>PS<sub>4-x</sub>Cl<sub>x</sub> (0 ≤ y ≤ x ≤ 0.2):** The phase identity was examined by powder X-ray diffraction (PXRD). The as-sintered pellets were ground into fine powders and placed in a holder, which was covered by a thin Kapton film to ensure a moisture- and oxygen-free environment. The PXRD patterns were acquired on a Philips X'Pert powder X-ray diffractometer at 45 kV and 40 mA at room temperature by using a Cu-Kα radiation (λ = 1.5406 Å) with a fixed scanning speed of 2° min<sup>-1</sup> from 15° to 60°. The morphologies of t-Na<sub>3.0</sub>PS<sub>3.8</sub>Cl<sub>0.2</sub> were

checked by scanning electron microscopy (SEM) on a NOVA NanoSEM 400 field-emission scanning electron microscope.

**Solid-State NMR:**  $^{23}\text{Na}$  solid-state NMR experiments were performed on a Bruker DRX-830 spectrometer (19.6T) with a home-built 3.2 mm low- $E$  and high-sensitivity MAS probe. The Larmor frequency of  $^{23}\text{Na}$  is 219.6 MHz.  $^{23}\text{Na}$  spectra were acquired using a single pulse with a solid  $90^\circ$  pulse length of 4.95  $\mu\text{s}$ , a recycle delay of 50 s, and a MAS rate of 16 kHz.  $^{23}\text{Na}$  spin-lattice relaxation time ( $T_1$ ) measurements were carried out with a saturation recovery pulse sequence.  $^{23}\text{Na}$  chemical shift was calibrated to 0.1 M NaCl solution at 0 ppm.  $^{31}\text{P}$  solid-state NMR spectra were obtained on a Bruker Avance III-500 spectrometer (11.75 T) with a 2.5 mm Bruker HXY MAS probe, operating at a Larmor frequency of 202.4 MHz.  $^{31}\text{P}$  spectra were acquired using a rotor-synchronized Hahn-echo pulse sequence with a  $90^\circ$  pulse length of 4.2  $\mu\text{s}$ , a recycle delay of 200 s, and a MAS rate of 25 KHz.  $^{31}\text{P}$  chemical shift was calibrated to 85%  $\text{H}_3\text{PO}_4$  solution at 0 ppm.

**Electrochemical Tests:** Ionic conductivities of  $\text{t-Na}_{3-y}\text{PS}_{4-x}\text{Cl}_x$  pellets at different temperatures were determined using AC impedance measurements. Indium (In) foils with a diameter of 5 mm were attached onto  $\text{t-Na}_{3-y}\text{PS}_{4-x}\text{Cl}_x$  pellets as blocking electrodes and current collectors. The sandwiched cell,  $\text{In}|\text{t-Na}_{3-y}\text{PS}_{4-x}\text{Cl}_x|\text{In}$ , was then sealed in a home-made cylindrical cell for tests. AC impedance measurements were performed on a Gamry Reference 600<sup>+</sup> potentiostat with a perturbation of 50 mV and a scanning frequency from 5 MHz to 1 Hz. Variable-temperature impedance measurements were performed from room temperature to 120  $^\circ\text{C}$ . Cyclic voltammetry measurements were carried out on  $\text{Na}|\text{t-Na}_{3-y}\text{PS}_{4-x}\text{Cl}_x|\text{In}$  between  $-0.5$  and 10 V at a scanning rate of 1 mV  $\text{s}^{-1}$ .

**Fabrication and Performance Evaluation of All-Solid-State Sodium-Ion Batteries:** A full cell was assembled using  $\text{Na}_3\text{V}_2(\text{PO}_4)_3/\text{C}$  as cathode, Na metal as anode, and  $\text{t-Na}_{3.0}\text{PS}_{3.8}\text{Cl}_{0.2}$  as solid electrolyte.  $\text{Na}_3\text{V}_2(\text{PO}_4)_3/\text{C}$  was prepared via a sol-gel process using citric acid as both chelating agent and carbon source.  $\text{V}_2\text{O}_5$ ,  $\text{NH}_4\text{H}_2\text{PO}_4$ ,  $\text{CH}_3\text{COONa}$ , and citric acid (molar ratio 1:3:3.15:2) were dissolved in deionized water first, and then the solution was continuously stirred at 80  $^\circ\text{C}$  to obtain a uniform gel. The gel was then heated at 350  $^\circ\text{C}$  for 5 h and at 800  $^\circ\text{C}$  for another 6 h in an argon atmosphere to obtain the final  $\text{Na}_3\text{V}_2(\text{PO}_4)_3/\text{C}$  cathode. The solid electrolyte  $\text{t-Na}_{3.0}\text{PS}_{3.8}\text{Cl}_{0.2}$  (50 mg) was cold-pressed using a 6 mm stainless steel die and then 5 mg composite cathode which contains 60%  $\text{t-Na}_{3.0}\text{PS}_{3.8}\text{Cl}_{0.2}$  and 40%  $\text{Na}_3\text{V}_2(\text{PO}_4)_3/\text{C}$  was pressed on top of the  $\text{t-Na}_{3.0}\text{PS}_{3.8}\text{Cl}_{0.2}$  electrolyte layer. Pure Na metal was pressed into a thin film which was attached to the opposite side of the  $\text{t-Na}_{3.0}\text{PS}_{3.8}\text{Cl}_{0.2}$  anode. The whole battery was sealed in a home-made cylindrical cell and cycled at current density of 10 mA  $\text{g}^{-1}$  calculated based on the mass of  $\text{Na}_3\text{V}_2(\text{PO}_4)_3$  within a voltage window of 2.5–3.8 V.

**DFT Calculations:** All DFT calculations were performed using the Vienna Ab initio Simulation Package (VASP)<sup>[20]</sup> within the projector augmented wave approach.<sup>[21]</sup> Similar parameters were used as previous works by the authors.<sup>[14,22,23]</sup> Briefly, all calculations were performed using the Perdew–Burke–Ernzerhof (PBE) generalized gradient approximation (GGA) functional.<sup>[24]</sup> For each composition (Na and Cl concentration), spin-polarized structure relaxation and total energy calculations of all symmetrically distinct configurations of  $\text{V}'_{\text{Na}}-\text{Cl}_5$  were performed in a  $2 \times 2 \times 2$  supercell of  $\text{t-Na}_3\text{PS}_4$  (16 formula units) using parameters consistent with those in Materials Project (MP),<sup>[25]</sup> that is, an energy cutoff of 520 eV and a k-point mesh of at least 1000/atom. The lowest energy configuration was then selected for the subsequent calculations and analyses.

Non-spin-polarized AIMD simulations were performed for  $\text{t-Na}_{3-y}\text{PS}_{4-x}\text{Cl}_x$  at  $x = 0.0625$  and 0.125 and  $y = 0, 0.0625$ , and 0.125 in an NVT ensemble at elevated temperatures with a Nose–Hoover thermostat.<sup>[26,27]</sup> A smaller plane-wave energy cutoff of 280 eV, a minimal  $\Gamma$ -centered  $1 \times 1 \times 1$  k-point mesh, and a time step of 2 fs were adopted. The simulation supercell sizes were around 14 Å ( $2 \times 2 \times 2$  supercell) along each lattice direction. The structures were fully relaxed at 0 K and the volumes were fixed for AIMD at elevated temperatures (800–1400 K). No framework melting was observed at the temperatures adopted in this study. The  $\text{Na}^+$  diffusivity was

calculated using the Einstein relation  $D = \frac{1}{2dt} \langle [\Delta \vec{r}(t)]^2 \rangle$ , where  $d$  is the dimensionality of diffusion (= 3 for 3D conductors here) and  $\langle [\Delta \vec{r}(t)]^2 \rangle$  is the average  $\text{Na}^+$  mean square displacement (MSD) over a time duration  $t$ . The diffusivity was obtained via a linear fitting of the MSD with time. Arrhenius plots were constructed to determine the activation energies and obtain extrapolated room-temperature diffusivities  $D_{300\text{K}}$ . The room-temperature Na-ion conductivity was derived from the Nernst–Einstein equation,  $\sigma_{300\text{K}} = \frac{\rho z^2 F^2}{RT} D_{300\text{K}}$ , where  $\rho$  is the molar density of diffusing Na ions in the unit cell;  $z = 1$  is the charge of Na ions; and  $F$  and  $R$  are the Faraday's constant and the gas constant, respectively.  $T = 300\text{K}$  was used in the above equation.

The Python Materials Genomics (pymatgen)<sup>[28]</sup> materials analysis library was used for all analyses and structure generation.

## Supporting Information

Supporting Information is available from the Wiley Online Library or from the corresponding author.

## Acknowledgements

This work was supported by the National Science Foundation under Grant No. DMR-1808517. All the NMR experiments were carried out at the NHMFL, which was funded by the state of Florida and NSF (DMR-1157490). The DFT studies were supported by the U.S. Department of Energy, Office of Science, Basic Energy Sciences under Award No. DESC0012118. The authors also acknowledge computational resources provided by Triton Shared Computing Cluster (TSCC) at the University of California, San Diego, the National Energy Research Scientific Computing Center (NERSC), and the Extreme Science and Engineering Discovery Environment (XSEDE) supported by National Science Foundation under Grant No. ACI-1053575.

## Conflict of Interest

The authors declare no conflict of interest.

## Keywords

all-solid-state sodium-ion batteries, functional defects, NMR, sodium solid electrolyte, thiophosphate

Received: November 8, 2018  
Revised: December 24, 2018  
Published online: January 18, 2019

- [1] Z. Yu, S.-L. Shang, J.-H. Seo, D. Wang, X. Luo, Q. Huang, S. Chen, J. Lu, X. Li, Z.-K. Liu, D. Wang, *Adv. Mater.* **2017**, *29*, 1605561.
- [2] W. D. Richards, T. Tsujimura, L. J. Miara, Y. Wang, J. C. Kim, S. P. Ong, I. Uechi, N. Suzuki, G. Ceder, *Nat. Commun.* **2016**, *7*, 11009.
- [3] N. Tanibata, K. Noi, A. Hayashi, M. Tatsumisago, *RSC Adv.* **2014**, *4*, 17120.
- [4] Z. Deng, Z. Wang, I.-H. Chu, J. Luo, S. P. Ong, *J. Electrochem. Soc.* **2016**, *163*, A67.
- [5] K. B. Hueso, M. Armand, T. Rojo, *Energy Environ. Sci.* **2013**, *6*, 734.
- [6] H.-P. Hong, *Mater. Res. Bull.* **1976**, *11*, 173.
- [7] O. Bohnke, S. Ronchetti, D. Mazza, *Solid State Ionics* **1999**, *122*, 127.



- [8] J. B. Goodenough, H.-P. Hong, J. A. Kafalas, *Mater. Res. Bull.* **1976**, *11*, 203.
- [9] A. Hayashi, K. Noi, A. Sakuda, M. Tatsumisago, *Nat. Commun.* **2012**, *3*, 856.
- [10] Z. Zhu, I.-H. Chu, Z. Deng, S. P. Ong, *Chem. Mater.* **2015**, *27*, 8318.
- [11] S.-H. Bo, Y. Wang, G. Ceder, *J. Mater. Chem. A* **2016**, *4*, 9044.
- [12] H. M. Tang, Z. Deng, Z. N. Lin, Z. B. Wang, I.-H. Chu, C. Chen, Z. Y. Zhu, C. Zheng, S. P. Ong, *Chem. Mater.* **2018**, *30*, 163.
- [13] M. Jansen, U. Henseler, *J. Solid State Chem.* **1992**, *99*, 110.
- [14] I.-H. Chu, C. S. Kompella, H. Nguyen, Z. Zhu, S. Hy, Z. Deng, Y. S. Meng, S. P. Ong, *Sci. Rep.* **2016**, *6*.
- [15] M. Duchardt, U. Ruschewitz, S. Adams, S. Dehnen, B. Roling, *Angew. Chem., Int. Ed.* **2018**, *57*, 1351.
- [16] J. Zheng, M. Tang, Y.-Y. Hu, *Angew. Chem., Int. Ed.* **2016**, *55*, 12538.
- [17] T. F. Willems, C. H. Rycroft, M. Kazi, J. C. Meza, M. Haranczyk, *Microporous Mesoporous Mater.* **2012**, *149*, 134.
- [18] S. Neuberger, S. P. Culver, H. Eckert, W. G. Zeier, J. Schmedt auf der Günne, *Dalton Trans.* **2018**, *47*, 11691.
- [19] Y. Kato, S. Hori, T. Saito, K. Suzuki, M. Hirayama, A. Mitsui, M. Yonemura, H. Iba, R. Kanno, *Nat. Energy* **2016**, *1*, 16030.
- [20] G. Kresse, J. Furthmüller, *Phys. Rev. B* **1996**, *54*, 11169.
- [21] P. E. Blöchl, *Phys. Rev. B* **1994**, *50*, 17953.
- [22] Z. Deng, Z. Zhu, I.-H. Chu, S. P. Ong, *Chem. Mater.* **2017**, *29*, 281.
- [23] Z. Zhu, I.-H. Chu, S. P. Ong, *Chem. Mater.* **2017**, *29*, 2474.
- [24] J. P. Perdew, K. Burke, M. Ernzerhof, *Phys. Rev. Lett.* **1996**, *77*, 3865.
- [25] A. Jain, S. P. Ong, G. Hautier, W. Chen, W. D. Richards, S. Dacek, S. Cholia, D. Gunter, D. Skinner, G. Ceder, K. A. Persson, *APL Mater.* **2013**, *1*, 011002.
- [26] S. Nosé, *J. Chem. Phys.* **1984**, *81*, 511.
- [27] W. G. Hoover, *Phys. Rev. A* **1985**, *31*, 1695.
- [28] S. P. Ong, W. D. Richards, A. Jain, G. Hautier, M. Kocher, S. Cholia, D. Gunter, V. L. Chevrier, K. A. Persson, G. Ceder, *Comput. Mater. Sci.* **2013**, *68*, 314.